The Astrophysical Journal, 869:13 (18pp), 2018 December 10 https://doi.org/10.3847/1538-4357/aaeacc
© 2018. The American Astronomical Society. All rights reserved.

Magnetohydrodynamic Simulation of the X9.3 Flare on 2017 September 6: Evolving Magnetic Topology

Chaowei Jiang[1,2,3], Peng Zou[1], Xueshang Feng[1,2], Qiang Hu[3], Rui Liu[4], P. Vemareddy[5], Aiying Duan[6], Pingbing Zuo[1,2], Yi Wang[1,2], and Fengsi Wei[1,2]

[1] Institute of Space Science and Applied Technology, Harbin Institute of Technology, Shenzhen 518055, People's Republic of China; chaowei@hit.edu.cn
[2] SIGMA Weather Group, State Key Laboratory for Space Weather, National Space Science Center, Chinese Academy of Sciences, Beijing 100190, People's Republic of China
[3] Center for Space Plasma and Aeronomic Research, The University of Alabama in Huntsville, Huntsville, AL 35899, USA
[4] CAS Key Laboratory of Geospace Environment, Department of Geophysics and Planetary Sciences, University of Science and Technology of China, Hefei 230026, People's Republic of China
[5] Indian Institute of Astrophysics, II-Block, Koramangala, Bengaluru-560034, India
[6] School of Atmospheric Sciences, Sun Yat-sen University, Zhuhai, Guangdong 519082, People's Republic of China
Received 2018 June 2; revised 2018 October 6; accepted 2018 October 8; published 2018 December 6

Abstract

Three-dimensional magnetic topology is crucial to understanding the explosive release of magnetic energy in the corona during solar flares. Much attention has been given to the pre-flare magnetic topology to identify candidate sites of magnetic reconnection, yet it is unclear how the magnetic reconnection and its attendant topological changes shape the eruptive structure and how the topology evolves during the eruption. Here we employed a realistic, data-constrained magnetohydrodynamic simulation to study the evolving magnetic topology for an X9.3 eruptive flare that occurred on 2017 September 6. The simulation successfully reproduces the eruptive features and processes in unprecedented detail. The numerical results reveal that the pre-flare corona contains multiple twisted flux systems with different connections, and during the eruption these twisted fluxes form a coherent flux rope through tether-cutting-like magnetic reconnection below the rope. Topological analysis shows that the rising flux rope is wrapped by a quasi-separatrix layer, which intersects itself below the rope, forming a topological structure known as a hyperbolic flux tube, where a current sheet develops, triggering the reconnection. By mapping footpoints of the newly reconnected field lines, we are able to reproduce both the spatial location and, for the first time, the temporal separation of the observed flare ribbons, as well as the dynamic boundary of the flux rope's feet. Furthermore, the temporal profile of the total reconnection flux is comparable to the soft X-ray light curve. Such a sophisticated characterization of the evolving magnetic topology provides important insight into the eventual understanding and forecasting of solar eruptions.

Key words: magnetic fields – magnetohydrodynamics (MHD) – methods: numerical – Sun: corona – Sun: flares

Supporting material: animations

1. Introduction

The Sun often produces major eruptive phenomena that impulsively release vast amounts of energy of the order of 10^{32} erg in a few minutes and strongly influence space weather. Such phenomena, observed as solar flares, filament eruptions, and coronal mass ejections (CMEs), are recognized to have a common driver—the magnetic field. This is because, in the solar corona, magnetic field plays a dominant role in the plasma dynamics, and solar eruptions are manifestation of sudden releases of free magnetic energy (Aschwanden 2004). Magnetic reconnection, which is associated with variation of magnetic field topology, is thought to be the central mechanism that leads to rapid dynamical evolution that ultimately converts free magnetic energy into radiation, energetic particle acceleration, and kinetic energy of plasma (Priest & Forbes 2002). Thus, unraveling the magnetic configuration of solar eruptions, and particularly the magnetic topology responsible for magnetic reconnection as well as its evolution during flares, is essential for understanding the nature of solar eruptions.

Without a direct measurement of the coronal magnetic field, many theoretical models of solar eruption have been proposed (Shibata & Magara 2011) to fit observations. For instance, the so-called standard flare model (i.e., the CSHKP flare model, Carmichael 1964; Sturrock 1966; Hirayama 1974; Kopp & Pneuman 1976) is most commonly invoked. When the magnetic configuration is of concern, this model provides simply a conceptual cartoon, in which a magnetic flux rope (MFR) in the corona, i.e., a bundle of twisted magnetic field lines lying above the polarity inversion line (PIL) of photospheric magnetic field and with their legs anchored at the photosphere, is ejected into the interplanetary space and forms a CME. Left behind, in the ejection's wake, is an electric current sheet (CS) formed between the stretched magnetic field lines tethering the MFR. The ejection's rise together with magnetic reconnection in its trailing CS release the stored magnetic energy. Nonthermal particles accelerated during the release of magnetic energy trace the newly reconnected field lines to the chromosphere, resulting in two parallel chromospheric flare ribbons on either side of the PIL. The temporal evolution of such a process is observed as a progressive separation of these two ribbons from each other as more and more flux reconnects.

The full 3D magnetic configuration and the dynamic evolution of solar eruptions are mostly investigated by numerical simulation based on the magnetohydrodynamics (MHD) model, which can describe well the macroscopic physical behavior of the solar corona. MHD simulation of a solar eruption with idealized magnetic configuration (that is, not directly constrained by observed magnetograms) has been reported in a number of papers (e.g., Mikic & Linker 1994; Amari et al. 2003; Linker et al. 2003; Roussev et al. 2003; MacNeice et al. 2004; Török & Kliem 2005; Fan & Gibson 2007; Aulanier et al. 2010; Kliem et al. 2010; Kusano et al. 2012; Török et al. 2013; Wyper et al. 2017; Mei et al. 2018). In particular, the evolution of the 3D magnetic topology of an MFR eruption has been extensively investigated in a series of papers (Aulanier et al. 2010, 2012; Janvier et al. 2014, 2015). It is found that a topological quasi-separatrix layer (QSL) wraps around the MFR and separates it from its ambient flux. Such a QSL consists of a continuous set of sheared magnetic field lines that defines the boundary surface of the rope, and reconnection occurs mainly below the rope, between the sheared arcades in a tether-cutting form (Moore et al. 2001); strictly speaking, this is slipping reconnection—see Figure 4 of Aulanier et al. (2010). The reconnection site is actually an intersection of the QSL with itself below the MFR, which forms a hyperbolic flux tube (HFT, Titov et al. 2002), and its 2D cross section corresponds to an X-point configuration. The photospheric footpoints of the QSL display two J-shaped ribbons, with the legs of the MFR anchored within the hooked parts. Thus reconnection in the QSL produces flare ribbons of J shapes, and with the separation of the main part of the ribbons, the hooks also expand. If the MFR is highly twisted, the hooks would close onto themselves, forming two rings as predicted by theoretical models (Demoulin et al. 1996), but this is not reproduced by the numerical model of Aulanier et al. (2010). Observation indeed shows such closed-ring-shaped ribbons connecting the ends of the two main ribbons. For instance, Wang et al. (2017) observed two closed-ring-shaped flare ribbons in the case of a buildup of highly twisted MFRs with the development of a flare reconnection. During the separation of the main flare ribbons, the flare rings expand significantly, starting from almost point-like brightening. Furthermore, transient coronal holes, i.e., post-eruptive coronal dimmings, are naturally suggested to map the feet of eruptive MFRs, along which mass leakage into interplanetary space could take place (Webb et al. 2000; Qiu et al. 2007).

Idealized MHD simulations are also commonly used to investigate the initiation mechanism of eruptions. Two kinds of ideal MHD instabilities have been commonly invoked as being the main driver of the eruption of an MFR. The first one, kink instability (KI, Hood & Priest 1981), depends on the degree of twist of the magnetic field line in the rope. MHD simulations suggest that KI occurs when the number of turns in the field lines around the rope axis exceeds a critical value of 1.75–2 (Fan & Gibson 2003; Török et al. 2004). Such a highly wound flux rope then evolves to reduce this strong internal twist by transferring some of its twist into writhe (deformation of the rope axis), conserving helicity in the process. The second one is the torus instability (TI, Kliem & Török 2006; Myers et al. 2015), which is a result of the loss of balance between the "hoop force" of the rope itself and the "strapping force" of the ambient field. The TI is determined by a decay index of the strapping field, which quantifies the decreasing rate of the strapping force with distance from the center of the torus. It is found that the TI occurs when the apex of the rope enters a domain with decay index larger than a threshold of $\sim$1.5, based on theoretical studies (Kliem & Török 2006) as well as MHD simulations (Fan & Gibson 2007; Aulanier et al. 2010).

Realistic simulation of solar eruptions constrained or driven by photospheric magnetograms (and other observable features) provides a significant step forward in understanding the complexity of magnetic configuration and evolution in real events. The power of simulations of this kind has been demonstrated by many authors (see a review by Inoue 2016). For instance, Jiang et al. (2013) simulated the sigmoid eruption in active region (AR) 11283, which possesses a complex configuration consisting of an MFR and a spine–fan null-point topology linking to multiple polarities. They first reconstructed an approximately nonlinear force-free field (NLFFF) model for the instant immediately prior to the eruption and found that the magnetic field is unstable (Jiang et al. 2013, 2014a). Then the unstable field is used to initialize a full MHD simulation, which can reproduce the subsequent eruption in remarkable agreement with the observed filament ejection. Jiang et al. (2016) further developed a data-driven MHD model that self-consistently follows the time-line of a flux-emerging AR over two days, leading finally to an eruption. Kliem et al. (2013) studied the eruption on 2010 April 8 by initializing their zero-β MHD model with an unstable pre-flare field model constructed by a flux-rope insertion technique (van Ballegooijen 2004; van Ballegooijen et al. 2007). It also yields good agreement with some observed features. Inoue et al. (2014) investigated the eruption mechanism of an X2.2 flare in the well-known AR 11158 (Sun et al. 2012). They first extrapolated an NLFFF model using a vector magnetogram observed by the Helioseismic and Magnetic Imager (HMI) on board the *Solar Dynamics Observatory* (*SDO*) two hours before the flare, and found that this NLFFF is stable in MHD simulation. Thus, an enhanced anomalous resistivity was used to increase the magnetic twist through tether-cutting reconnection in those sheared arcades in the AR core, after which the quasi-equilibrium was broken and an eruption followed. Similar approaches are also adopted in Amari et al. (2014, 2018) and Inoue et al. (2018).

Based on these data-constrained and data-driven simulations, the evolution of the 3D magnetic topology and its relation with observed flare ribbons were investigated recently. Using the flux-rope insertion method, Savcheva et al. (2015) modeled the magnetic field of seven two-ribbon flares and found that the main ribbons are matched well by the flux-rope-related QSLs except for some parts of the hooks of the J-shaped ribbons. Savcheva et al. (2016) further studied the evolution of unstable flux-rope models using their magnetofrictional code and showed that the evolution of flare ribbons can also be partially reproduced by tracking the evolution of the flux-rope-related QSLs. In the data-driven simulation of a flux-emergence process that leads finally to eruption, Jiang et al. (2016) found that during the emergence a null-point-like magnetic topology is formed with a quasi-circular QSL whose footpoints match the observed quasi-circular flare ribbon. The same data-driven model was used to study the great confined flare of X3.1 in super AR 12192 (Jiang et al. 2016), and a strikingly good match of the reconnecting field-line footpoint with flare ribbons was achieved, but only a snapshot in time was shown. Very recently, Jiang et al. (2017) modeled the magnetic field of a peculiar X-shaped-ribbon flare and found that a large-scale CS

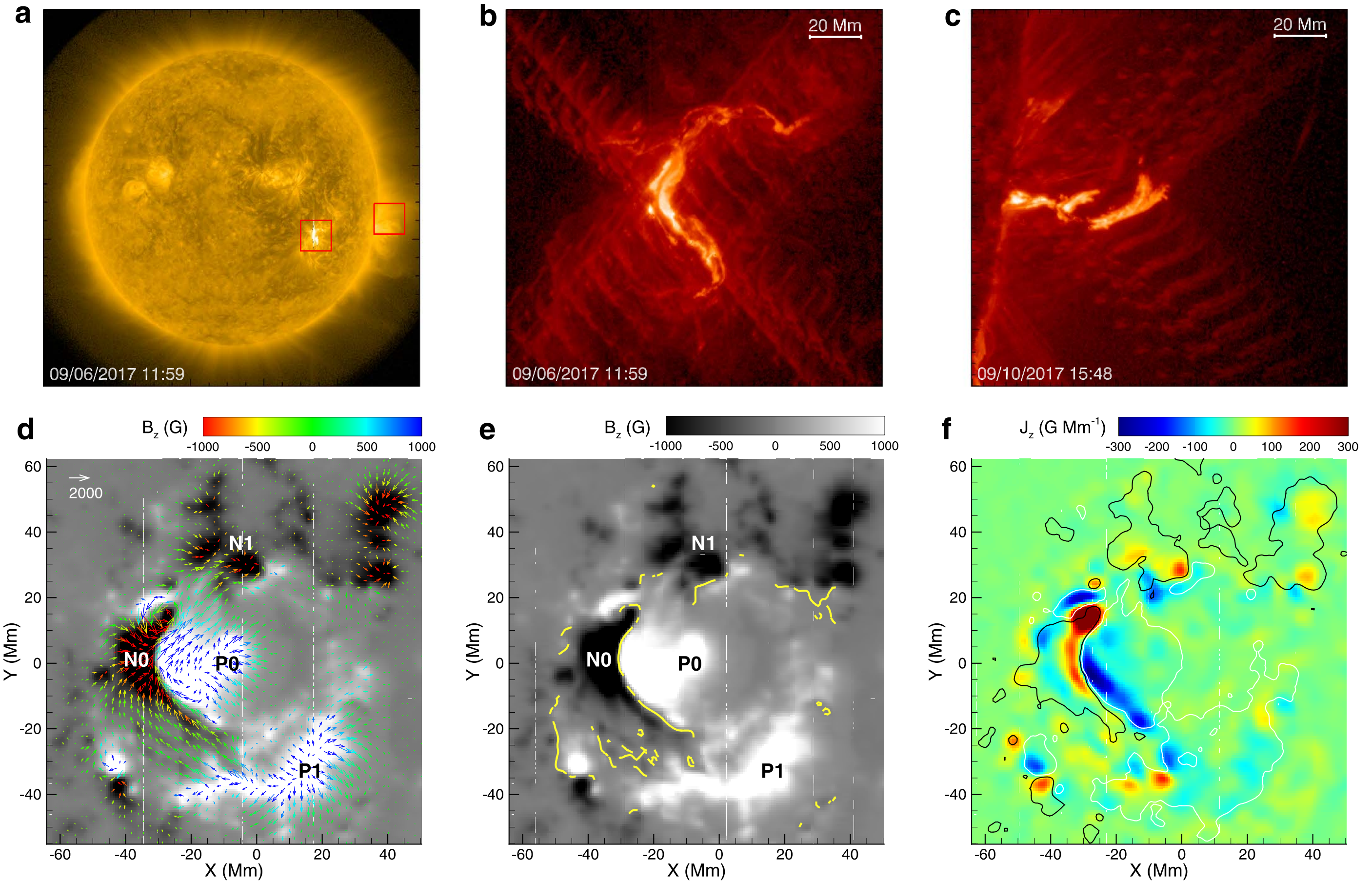

Figure 1. The flare location and photospheric magnetic field. (a) Full-disk image of the Sun observed with *SDO*/AIA 171 Å. The two boxes indicate the locations of the on-disk X9.3 flare on September 6 and the limb X8.2 flare that occurred on September 10. (b) and (c) *SDO*/AIA 304 Å images of the X9.3 flare and the X8.2 flare, respectively. (d)–(f) *SDO*/HMI vector magnetograms taken at 11:36 UT on September 6, which is 17 minutes before the onset of the X9.3 flare. In (d), the magnetic flux distribution, i.e., B_z, is overlaid by the transverse field vector (B_x, B_y) as denoted by the colored arrows. The main magnetic polarities P0, N0, P1, and N1 are labeled. In (e) the yellow curves are the locations of bald patches along the PIL. (f) Distribution of the vertical current density, which is defined as $J_z = \partial_x B_y - \partial_y B_x$. The contour lines are plotted for $B_z = -500$ G (colored black) and 500 G (white). The ratio of the direct current (DC) to the return current (RC) for the positive flux is $|\mathrm{DC/RC}|^+ = 2.31$, and for the negative flux it is $|\mathrm{DC/RC}|^- = 2.26$.

existing prior to the flare and the footpoints of field lines tracing from the CS reproduces the shape of the ribbons.

This paper is devoted to a comprehensive analysis of the 3D magnetic configuration and evolution of the great eruptive flare that occurred on 2017 September 6 with a data-constrained MHD simulation. The studied flare, reaching *GOES* X9.3 class (*GOES* is the *Geostationary Operational Environmental Satellite*), was the largest one in the past decade and quickly drew great attention in the communities of solar physics (Sun & Norton 2017; Yang et al. 2017; Huang et al. 2018; Li et al. 2018; Wang et al. 2018; Warren et al. 2018; Yan et al. 2018) as well as space weather (e.g., Lei et al. 2018). The flare occurred in a magnetic complex due to the interaction of multiple magnetic polarities as observed on the photosphere. Our MHD simulation realistically reproduces the dynamic evolution of the magnetic field underlying the flare. In particular, we focus on the magnetic topology and its evolution during the flare. Our model of the field at the time of the X9.3 flare contains a complex and unstable MFR system, which is possibly due to the TI, and the eruption results from the consequent expansion of the MFR. Furthermore, with an accurate analysis of the topology, we find that the footpoint of those field lines reconnected underneath the MFR roughly matches both the spatial location and the temporal evolution of flare ribbons. We will first describe data and models in Section 2, then present the simulation results and compare them with observations in Section 3, and finally conclude in Section 4.

2. Data and Models

2.1. Event and Data

The investigated flare SOL2017-09-06T11:53, which is the largest flare in solar cycle 24, took place in a super flare-productive solar AR, NOAA 12673. In this AR, four X-class and 27 M-class flares were produced from 2017 September 4 to 10. The X9.3 flare on September 6 started at 11:53 UT, impulsively reached its peak at 12:02 UT, and then ended at 12:10 UT, and was accompanied by a large CME (Yan et al. 2018). Its location on the solar disk is shown in Figure 1, as imaged by the Atmospheric Imaging Assembly (AIA) on board the *SDO*. The *SDO*/AIA can provide a full-disk image of the Sun simultaneously in six EUV filters: 171, 193, 211, 335, 94, and 131 Å. The spatial resolutions of all these filters are 0.6 arcsec and the cadences are 12 s.

When AR 12673 rotated to the solar limb on 2017 September 10 (Figure 1(c)), it produced an X8.2 flare, which is the second largest one after the X9.3 flare. As the two flares are generated in the same region, they might plausibly have basically the same 3D magnetic configuration. Thus the observation of this limb flare provides a side view of the 3D structure underlying the flares, in addition to the nearly top view for the X9.3 flare. The AIA image of this limb flare will be used to compare qualitatively with our simulation of the X9.3 flare in a 2D slice.

The vector magnetogram used for our coronal field extrapolation is taken by the HMI (Schou et al. 2012) on board *SDO*. In particular, we used the data product of the Space-weather HMI Active Region Patch (SHARP, Bobra et al. 2014), in which the 180° ambiguity has been resolved by using the minimum energy method, the coordinate system has been modified via the Lambert method, and the projection effect has been corrected. The magnetogram for this AR is well flux-balanced because the ratio of the total flux to the total unsigned flux is ∼0.05. Since this flare was associated with an erupting filament, the Hα data with a spatial resolution of 1 arcsec from the Global Oscillation Network Group (GONG) are used as well for checking the location of the filament.

2.2. NLFFF Model

The pre-flare coronal magnetic field is extrapolated by our CESE–MHD–NLFFF code (Jiang & Feng 2013). It belongs to the class of MHD relaxation methods that seek approximately force-free equilibrium:

$$(\nabla \times \boldsymbol{B}) \times \boldsymbol{B} = 0 \tag{1}$$

for a given boundary value specified by observed vector magnetograms. It solves a set of modified zero-β MHD equations with a friction force using an advanced conservation-element/solution-element (CESE) spacetime scheme on a non-uniform grid with parallel computing (Jiang et al. 2010). Starting from a potential field extrapolated from the vertical component of the vector magnetogram, the zero-β MHD system is driven to evolve by incrementally changing the transverse field at the bottom boundary until the vector magnetogram is matched, after which the system will be relaxed to a new equilibrium. In the code, a pseudo plasma density $\rho = B^2$ is used in the momentum equation. We use two terms in the induction equation to control the nonzero magnetic divergence: one is the Powell source term $-\boldsymbol{v}\nabla \cdot \boldsymbol{B}$ (Powell et al. 1999), and the other is a diffusion term $\nabla(\mu\nabla \cdot \boldsymbol{B})$ where μ is the diffusion coefficient. These two terms can effectively control the numerical magnetic divergence. The code has an option of using adaptive mesh refinement and a multi-grid algorithm for optimizing the relaxation process (Jiang & Feng 2012). The computational accuracy is further improved by a magnetic-field splitting method, in which the magnetic field is divided into a potential-field part and a non-potential-field part, and only the latter is actually evolved in the MHD relaxation to derive the NLFFF field. Before being input into the code, the raw vector magnetogram is required to be preprocessed to reduce the Lorentz force it contains. Furthermore, to be consistent with the code, we developed a unique preprocessing method (Jiang & Feng 2014) that also splits the vector magnetogram into a potential part and a non-potential part and handles them separately. Then the non-potential part is modified and smoothed by an optimization method similar to that of Wiegelmann & Neukirch (2006) to fulfill the conditions of being totally magnetic force-free and torque-free. The preprocessing alters the original HMI magnetogram in all three components. A simple way to convey the extent of the changes is to compute planar (2D) versions of the quantities defined by Equations (28)–(31) in Schrijver et al. (2006). These are: $C_{\rm vec} = 0.95$, $C_{\rm cs} = 0.69$, $E_{\rm n} = 0.38$, $E_{\rm m} = 0.72$. Ideally, the first two would be 1.0, and the latter would be zero. These discrepancies are mostly due to the smoothing of the data. Details of the CESE–MHD–NLFFF code and the preprocessing method are described in a series of papers (Jiang et al. 2013, 2014a, 2014b; Jiang & Feng 2014). They are well tested by different benchmarks including a series of analytic force-free solutions (Low & Lou 1990) and numerical MFR models (Titov & Démoulin 1999; van Ballegooijen 2004), and have been applied to the *SDO*/HMI vector magnetograms (Jiang & Feng 2013; Jiang et al. 2014a); they are able to reproduce magnetic configurations in very good agreement with corresponding observable features, including coronal loops, filaments, and sigmoids.

2.3. MHD Model

The MHD simulation is realized by solving the full set of 3D, time-dependent ideal MHD equations with solar gravity. The initial condition consists of the magnetic field provided by the NLFFF model and a hydrostatic plasma. While the NLFFF derivation procedure only solved for $\boldsymbol{B}$ and $\boldsymbol{v}$ in a pseudo-evolution, in the MHD model of the eruption all MHD variables (ρ, $\boldsymbol{v}$, $\boldsymbol{B}$, p) are solved for. The initial temperature is uniform, with a value typically in the corona of $T = 10^6$ K (which gives sound speed $c_S = 128\ {\rm km\ s^{-1}}$). The initial plasma density is uniform in the horizontal direction and vertically stratified by gravity. To mimic the coronal low-β and highly tenuous conditions, the plasma density is configured to make the plasma β less than 0.1 in most of the computational volume. The smallest value of β is 5×10^{-4}, corresponding to the largest Alfvén speed $v_{\rm A}$ of approximately 8 ${\rm Mm\ s^{-1}}$. The units of length and time in the model are $L = 11.5$ Mm (approximately 16 arcsec on the Sun's disk) and $\tau = L/c_S = 90$ s, respectively. In this simulation, the MHD code was run for 1 τ. The MHD solver is the same CESE code described in Jiang et al. (2010). We use a non-uniform grid with adaptive resolution based on the spatial distributions of the magnetic field and current density in the NLFFF model. This grid is designed to save computational resources without losing numerical accuracy, and more details of this can be found in Jiang et al. (2017). The smallest grid is $\Delta x = \Delta y = 2\Delta z = 0.36$ Mm (approximately 0.5 arcsec on the Sun). A moderate viscosity ν, which corresponds to a Reynolds number $R_e = Lv_{\rm A}/\nu\ \sim\ 10^2$, is used to keep the numerical stability of the code running for the whole duration of the flare eruption process. No explicit resistivity is included in the magnetic induction equation, and magnetic reconnection is still allowed due to numerical resistivity η, which corresponds to the Lundquist number (or magnetic Reynolds number) $S = Lv_{\rm A}/\eta \sim 5 \times 10^3$ in our grid settings and numerical scheme. Although there is no doubt that the viscosity and numerical resistivity in our model overestimate the real values in the coronal plasma (which are of the order of 10^8–10^{10}), the basic evolution of the magnetic topology as simulated is still robust (see also Jiang et al. 2016). The computational volume is slightly larger than the size of simulated AR, and the simulation is stopped before any disturbance reaches the numerical boundaries. At the bottom boundary (i.e., the coronal base), all the variables are fixed (thus the density and temperature are constant in both time and space, and the velocities are held at zero) except the transverse components of the magnetic field, which are released (or floated) by linear extrapolation from the inner points along the z-axis.

In the combination of the NLFFF model and MHD simulation, it should be noted that almost all the available NLFFF codes actually generate non-force-free magnetic field data with residual Lorentz forces that are often non-negligible. In our code, some of the residual forces in this NLFFF procedure will arise from the artificial friction used in the method. The magnitude of these residual forces can be indicated by the misalignment of the current $\boldsymbol{J}$ and magnetic field vector $\boldsymbol{B}$ (Schrijver et al. 2006), which is usually measured by CWsin, a current-weighted average sine of the angle between $\boldsymbol{J}$ and $\boldsymbol{B}$. CWsin is typically in the range of 0.2 to 0.4 (see, e.g., Schrijver et al. 2008; DeRosa et al. 2009, 2015). Another metric $E_{\nabla\times\boldsymbol{B}}$ measuring the residual Lorentz force more directly is defined as the average ratio of the force to the sum of the magnitudes of magnetic tension and pressure forces (Duan et al. 2017). In the event studied here, these two metrics for the CESE–MHD–NLFFF extrapolation are respectively, CWsin = 0.23 and $E_{\nabla\times\boldsymbol{B}} = 0.17$. These metrics are reasonably small as compared with other codes (e.g., see the last column of Table 2 in DeRosa et al. 2015), but such residual force can instantly induce plasma motion in a low-β and highly tenuous plasma environment. Actually, this initial motion provides a way of perturbing the system. If the system is very stable, i.e., significantly far away from an unstable regime, it will quickly relax to MHD equilibrium because the induced motion can alter the magnetic field, which in turn generates a restoring force to brake the motion. Otherwise, if the system is unstable or not far away from an unstable regime, the perturbation could grow and lead to a drastic evolution of the system as driven by the instability. Thus the combination of NLFFF and the MHD model can be used to test the potentially unstable nature or instability of numerical NLFFF, while here we cannot assess exactly what mechanisms make the extrapolated field unstable. Nevertheless, it still provides a viable tool to reproduce the fast magnetic evolution during the flare.

2.4. Magnetic Field Analysis Method

We used a set of magnetic field analysis methods including a search for magnetic bald patches (BPs, Titov et al. 1993), and calculation of magnetic twist number, squashing degree, and decay index, which are described in the following.

BPs are places on the photospheric PIL where the transverse field is directed from negative polarity to positive. This is inverse to the normal case in which the transverse field is directed from positive flux to negative, and thus the field line is concave upward. BPs are special because they define a magnetic topology separatrix, known as a BP separatrix surface (BPSS, Titov & Démoulin 1999), which is often associated with an MFR that is attached to the photosphere. BPs can be located by searching for the point on the magnetogram where the conditions

$$\boldsymbol{B}\cdot\nabla B_z > 0,\ \ B_z = 0 \tag{2}$$

are satisfied. Magnetic dips are searched for using the same conditions but applied to the full 3D volume of the field.

The magnetic twist number T_w for a given (closed) field line is defined by (Liu et al. 2016)

$$T_w = \int_L \frac{(\nabla\times\boldsymbol{B})\cdot\boldsymbol{B}}{4\pi B^2}dl \tag{3}$$

where the integral is taken along the length L of the magnetic field line from one footpoint to the other. To be precise, T_w measures the number of turns that two infinitesimally close field lines wind about each other (Liu et al. 2016).

The squashing degree Q is derived based on the mapping of two footpoints for a field line. Specifically, a field line starts at one footpoint $(x,\ y)$ and ends at the other footpoint $(X(x,\ y),\ Y(x,\ y))$. Then the squashing degree associated with this field line is given by (Titov et al. 2002)

$$Q = \frac{a^2+b^2+c^2+d^2}{|ad-bc|} \tag{4}$$

where

$$a = \frac{\partial X}{\partial x},\ \ b = \frac{\partial X}{\partial y},\ \ c = \frac{\partial Y}{\partial x},\ \ d = \frac{\partial Y}{\partial y}. \tag{5}$$

Usually QSLs can be defined as locations where $Q \gg 2$.

In the TI (Kliem & Török 2006), which is a result of the loss of balance between the "hoop force" of the rope itself and the "strapping force" of the ambient field, the decay index n plays a key role. It quantifies the decreasing strength of the strapping force along the distance from the center of the torus. Here n is calculated in the vertical cross section that perpendicularly crosses the main axis of the rope (see Figure 3(c)) in such a manner: we regard the bottom PIL point, named O (denoted by the black circle in the figure) as the center of the torus, and for a given grid point P, $n(\mathrm{P}) = -d\log(B_\mathrm{p})/d\log(h)$, where B_p is the magnetic field component perpendicular to the direction vector $\boldsymbol{r}_\mathrm{OP}$, and $h = |\boldsymbol{r}_\mathrm{OP}|$. Here the strapping field is approximated by the potential field model that matches the B_z component of the photospheric magnetogram (Aulanier et al. 2010; Jiang et al. 2013). The TI occurs when the apex of the rope enters a domain with decay index larger than a threshold of ∼1.5 based on theoretical studies (Kliem & Török 2006).

3. Results

3.1. Magnetic Field on the Photosphere

First, we analyzed the pre-flare magnetic field in the photosphere observed by *SDO*/HMI at the time 11:36 UT, just 17 minutes ahead of the onset of the flare. This vector magnetogram provides the only input to our numerical models. As shown in Figure 1(d), there are four main magnetic concentrations. In the core region, two closely touching magnetic concentrations of opposite polarity, P0 and N0, are separated by a PIL of C shape (referred to as the main PIL hereafter), and almost enclosed by another two concentrations (P1 and N1) to the south and north, respectively. Analysis of the time-sequence magnetograms suggested that such a configuration is formed by several groups of extremely fast emerging flux blocked by a pre-existing sunspot (Yang et al. 2017), which results in a strongly distorted magnetic system. Significant magnetic shear can be seen along the main PIL, which is so strong that magnetic BPs form on almost the whole PIL (Figure 1(e)). The presence of BPs means that magnetic field lines immediately above the PIL do not connect P0–N0 directly but are concave upward, grazing over the PIL and

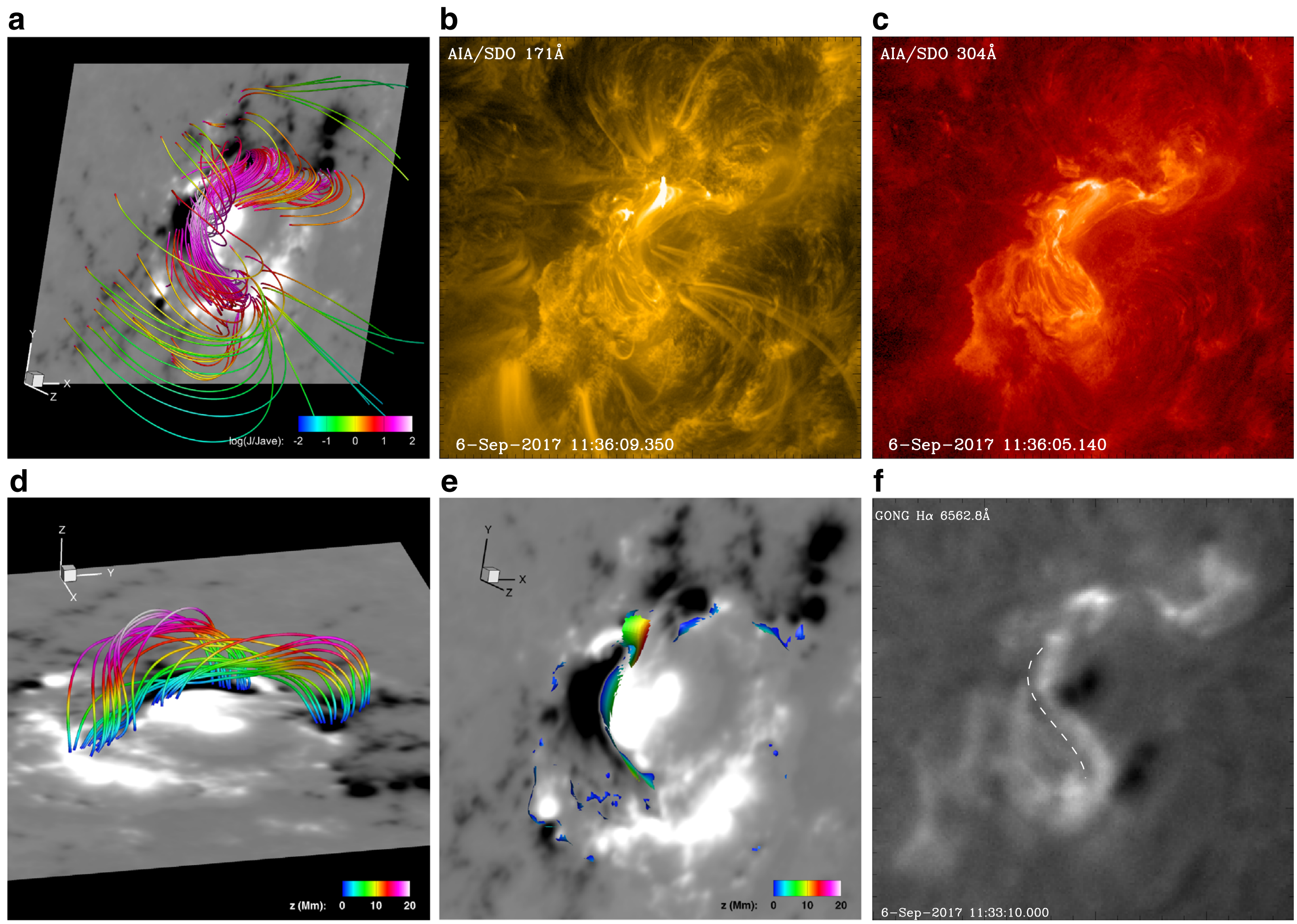

Figure 2. Comparison of the reconstructed magnetic field with the observed features of the solar corona prior to the flare. (a) *SDO* view of sampled magnetic field lines of the NLFFF reconstruction. The color of the lines represents the value of current density J (normalized by its average value J_{ave} in the computational volume). The background is the photospheric magnetogram. (b) and (c) *SDO*/AIA 171 Å and 304 Å images of the pre-flare corona. (d) The low-lying magnetic field lines in the core region. The field lines are color-coded by the value of height z. (e) Locations of dips in the magnetic field lines; the color indicates the value of height z. (f) GONG Hα image of the AR. The dashed curve denotes the location of a long filament.

forming magnetic dips. Such a magnetic-sheared configuration with BPs is often found in the case of theoretical models of a coronal MFR that is partially attached to the photosphere (Gibson & Fan 2006; Aulanier et al. 2010).

Strong current can be seen directly from the transverse magnetic field. For example, the transverse magnetic vectors form a distinct vortex in the north end of N0, indicating strong current and magnetic twist there. Indeed, a distribution of enhanced electric currents with opposite directions on either side of the main PIL is derived through Ampère's law from the transverse magnetic field (Figure 1(f)), which indicates that volumetric current channels through the corona like a closed circuit (Janvier et al. 2014; Sun et al. 2015). The current is significantly non-neutralized with respect to magnetic flux of either sign: the ratio of the direct current (DC) to the return current (RC) for the positive flux is $|\mathrm{DC/RC}|^{+} = 2.31$, and for the negative flux it is $|\mathrm{DC/RC}|^{-} = 2.26$. Such non-neutralized current has recently been recognized to be a common feature of many eruptive ARs (Kontogiannis et al. 2017; Liu et al. 2017; Vemareddy 2017), and supports the idea that an MFR exists prior to eruption (Török et al. 2014). All these features suggest that a twisted MFR exists in the region and can likely account for the eruptive activities.

3.2. Pre-flare Coronal Magnetic Configuration

The coronal magnetic field in a quasi-static state prior to a flare can be well approximated by force-free models. From the HMI vector magnetogram, our NLFFF code reconstructs magnetic field lines that nicely match the observed coronal loops (see Figure 2). The pre-flare magnetic configuration comprises a set of strongly sheared (current-carrying) low-lying (heights of $\sim$10 Mm) field lines in the core region, which is enveloped by less sheared arcades (Figures 2(a) and (d)). The low-lying field lines extend their ends to the south and north polarities P1 and N1, forming an overall C shape. Concave-upward portions of these field lines, also termed magnetic dips, are able to support dense filament material against the solar gravity. As shown in Figure 2(e), the dips are distributed almost all the way along the main PIL, which is consistent with the distribution of BPs. They can thus support a long filament along the PIL. Such a filament appears to exist, as seen in the GONG Hα image (Figure 2(f)), and the shape of the dips matches the filament rather well.

The existence of an MFR is confirmed by the NLFFF model. Calculation of the magnetic twist number T_w shows that the

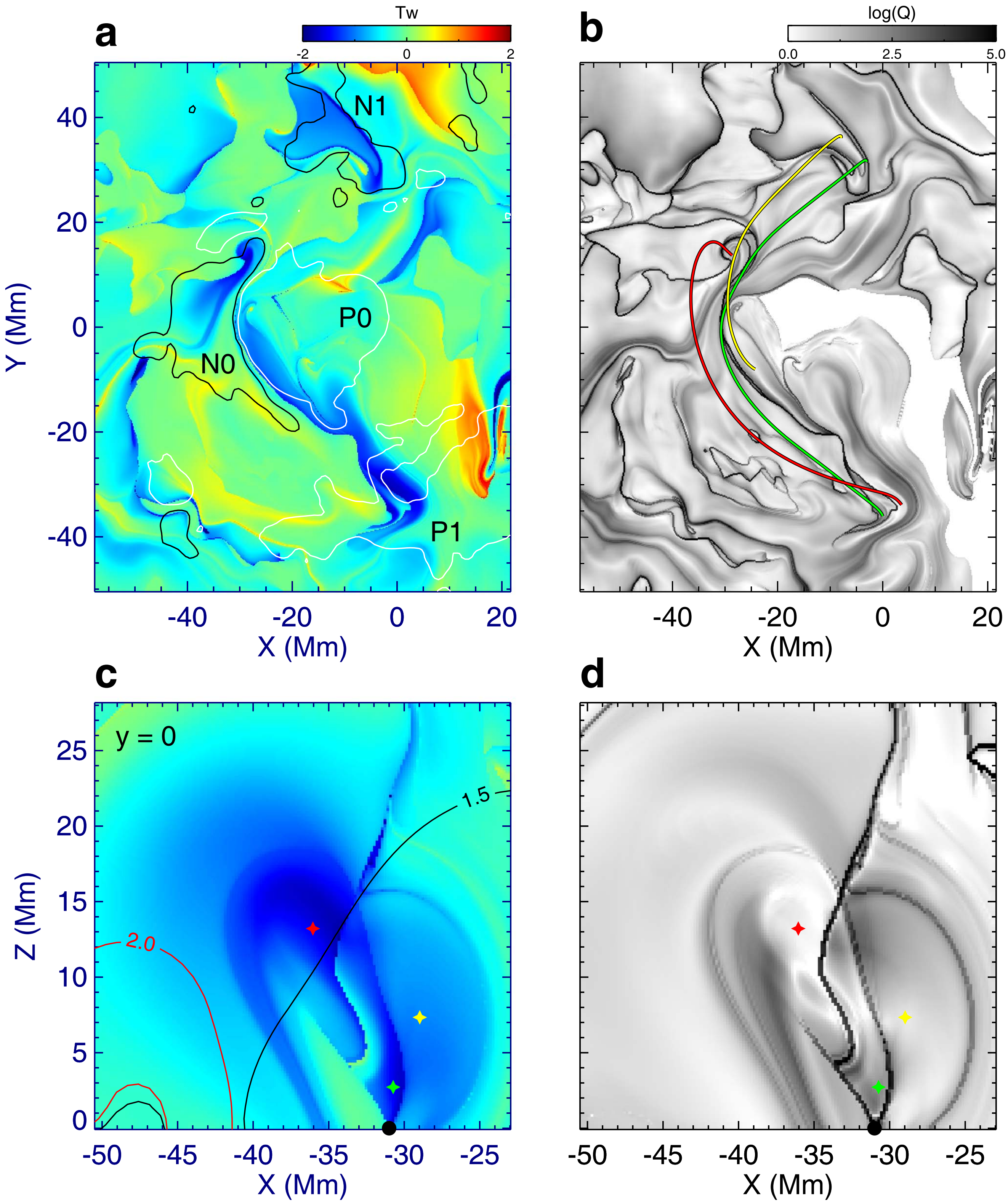

Figure 3. Detailed configuration of the reconstructed pre-flare magnetic field. (a) Map of magnetic twist number T_w at the bottom surface $z = 0$. Overlaid are contour lines for $B_z = 500$ G (white) and -500 G (black). Coordinates are the same as shown in Figure 1(d). (b) Map of magnetic squashing factor Q at the bottom. The black thin lines formed by large Q values are locations of magnetic topology separatrices and QSLs where the magnetic field-line mapping is discontinuous or changes rapidly. Three field lines with different colors are plotted to represent the magnetic flux of the different connections that make up the MFR. (c) Distribution of twist number in a vertical cross section ($y = 0$). The three colored stars denote the intersection points of the sample field lines shown in (b) with the cross section. The black circle indicates the main PIL. The contour lines are shown for the decay index $n = 1.5$ and 2. (d) Distribution of magnetic squashing factor Q in the same cross section shown in (c).

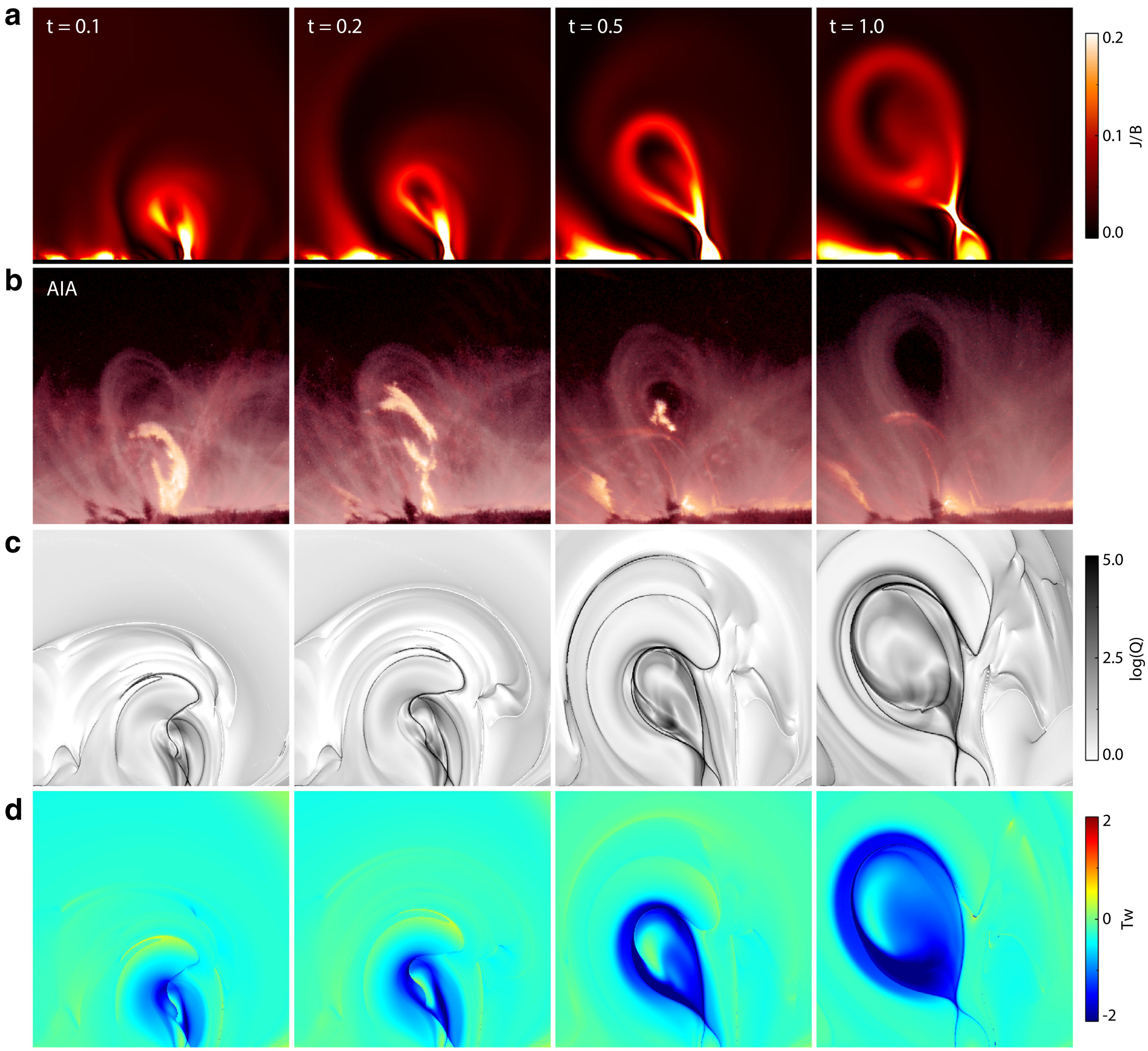

Figure 4. Temporal evolution of the eruptive structure in a 2D view. (a) Distribution of current density on the vertical cross section (the $y = 0$ plane). Here the current density is normalized by local magnetic field strength, which provides a high contrast of thin current layers with other volumetric currents. The unit of J/B is $1/\Delta$ where Δ is the grid size. (b) *SDO*/AIA images of the X8.2 flare observed at the solar limb. The images are made by a combination of the two AIA channels 211 Å and 304 Å, and they are rotated to roughly match the direction of the simulated eruption. (c) and (d) Distributions of magnetic squashing degree Q and twist number T_w, respectively, in the same cross section as in (a).

low-lying core field is twisted left-handedly (see Figure 3). The magnetic twist number ($T_w < 0$) is significantly enhanced along the two sides of the main PIL, nearly at the locations of intense current density (compare Figures 1(f) and 3(a)). The regions of enhanced negative twist also extend to the far-side polarities P1 and N1. The magnetic twist number in most of these regions is to be around 1.5, which is close to the threshold of KI for an idealized MFR (Török et al. 2004). Here the twisted magnetic flux constitutes a complex flux-rope configuration with multiple domains of connectivity. The different connections can be distinguished from a map of magnetic squashing degree (the Q factor) (Demoulin et al. 1996; Titov et al. 2002), which precisely maps the topological separatrices or QSLs of the field-line connectivity. As shown in Figure 3(b), this twisted flux bundle consists of mainly three types of connections: P1–N0, P0–N1, and P1–N1, while the connection of P0–N0 does not form along the main PIL, as a natural result of the existence of the BPs. Note that the flux connection of P1–N1 is bounded at each footpoint by a closed high-Q line, the footpoint of the QSL wrapping around the flux rope (Figure 3(b)). In a vertical cross section (Figure 3(d)), this QSL touches the bottom surface, also because of the presence of BPs there. A true separatrix, i.e., BPSS, exists at the center of this QSL where $Q \to \infty$. As shown by the distribution of twist number in the cross section $y = 0$ (Figure 3(c)), the MFR is not

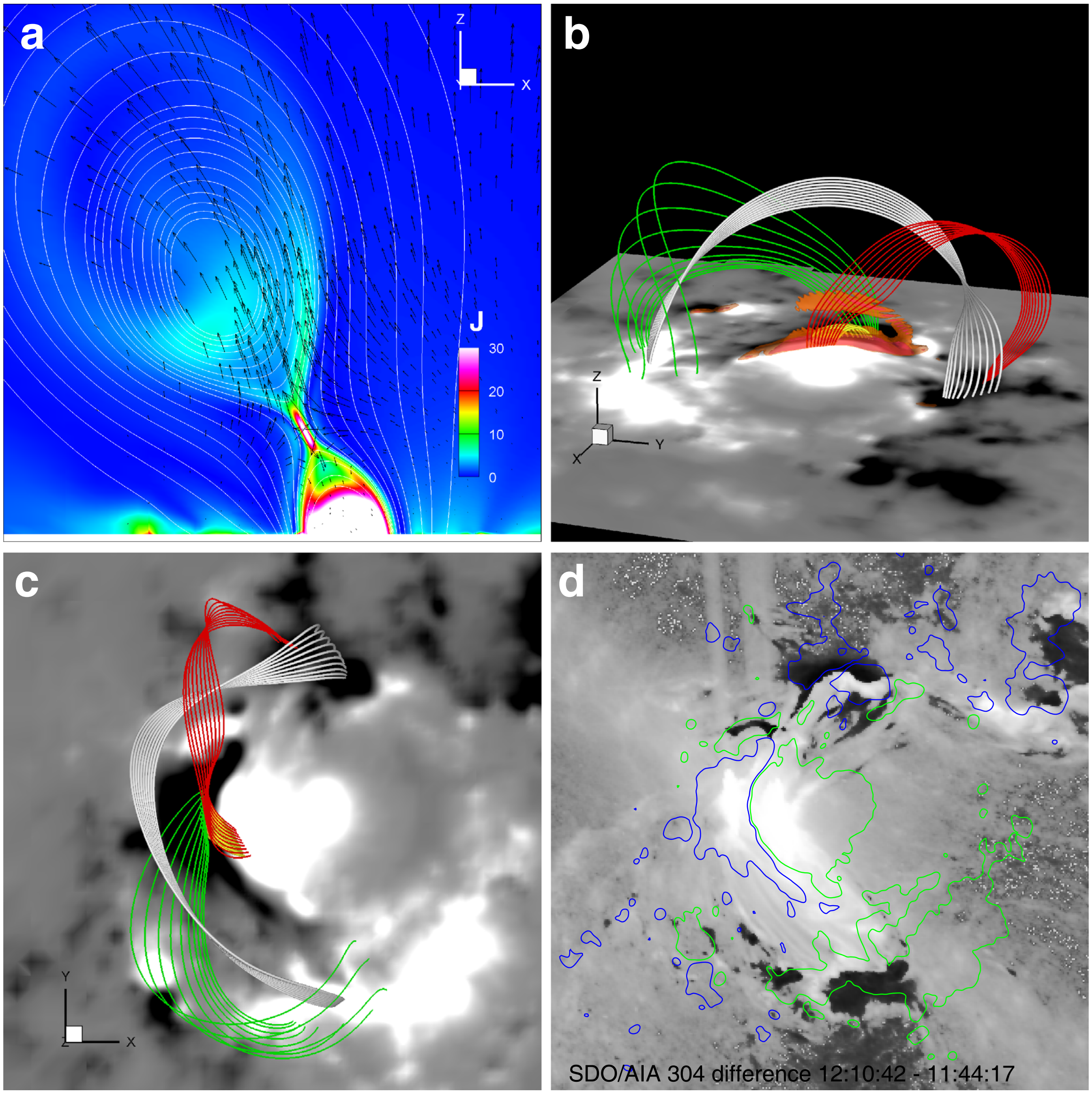

Figure 5. Illustration of the reconnection process below the rising MFR. (a) Current density distribution and plasma flows (denoted by arrows) on the vertical cross section (the $y = 0$ plane) at time $t = 1.0$. The white lines are 2D field lines tracing on the plane. (b) 3D configuration of the reconnection. The white lines are within the main body of the MFR. The red and green lines are reconnecting field lines below the rope. Their inner footpoints are sheared past each other along the PIL, and thus the field directions change abruptly across the CS, in which reconnection takes place, resulting in a long field line joining the MFR and a short arcade below which the post-flare loops form (as shown by the yellow lines). The objects colored in red and orange are thin layers with the strongest current density throughout the volume, showing the CS in 3D. (c) Top view of the same magnetic field lines shown in (b). (d) Difference of AIA 304 Å images before and after the flare, showing two dimming sites (or transient coronal holes) that match the locations of the MFR legs. The contour lines are shown for $B_z = -500$ G (colored in blue) and 500 G (colored in green).

uniformly twisted (for instance, part of the P1–N1 connection has a twist of only ∼0.5), nor is it a coherent structure with a well-defined rope axis. We note that such multiple connections and inhomogeneous twist are not characterized by any theoretical (or idealized) models of MFR, but are often found in NLFFF reconstructions (e.g., Awasthi et al. 2018).

We further compute the decay index n of the strapping field, which is the key parameter determining the TI of an MFR system. In the idealized model, the TI occurs once the apex of the rope axis reaches the domain of $n > 1.5$ (Kliem & Török 2006; Aulanier et al. 2010), but here there is no well-defined axis. Despite this, it is found that the major part of the MFR (i.e., the flux with $|T_w| > 1$) reaches a region with $n > 1.5$ (see Figure 3(c)). This indicates that the MFR is already in an unstable regime, suggesting that the eruption is more likely a result of TI rather than KI. However, a conclusion cannot be drawn here because the TI (and KI) theory is derived from idealized MFR configurations, while our realistic coronal field is much more complex. Thus, we note that it is still unclear what exactly the unstable nature of the pre-flare field is.

3.3. The Eruptive Evolution

The eruption is characterized by a drastic rise and expansion of the MFR in the MHD simulation, which is shown in Figure 4 for a vertical cross section. As clearly seen from the cross section of current density (J/B, Figure 4(a)), a narrow

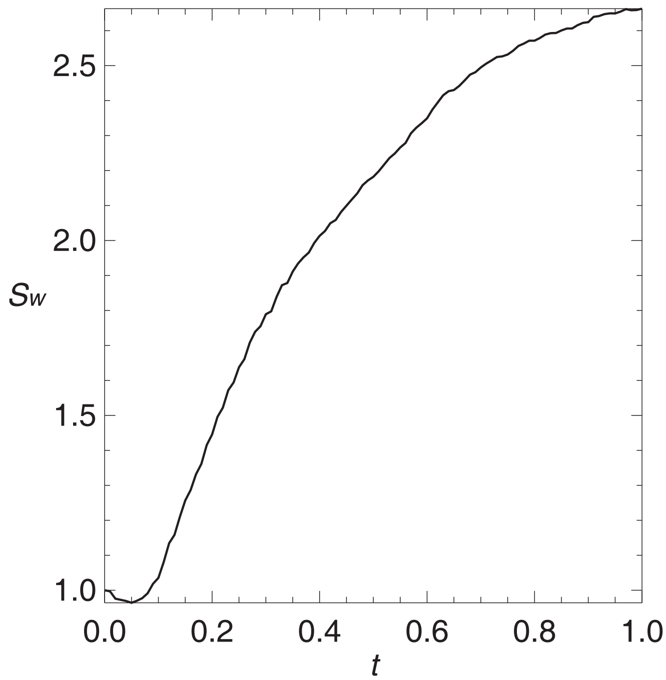

Figure 6. Evolution of twisted flux content. The magnetic flux content S_w of the MFR is calculated as $S_w = \int |T_w B_y| dxdz$ on the surface $y = 0$, and the integration is limited to the area with $|T_w| > 1$. The number S_w as shown is normalized by its initial value at $t = 0$.

current layer of upside-down teardrop shape forms at the boundary the MFR. Such a boundary is precisely depicted by a QSL, as shown in the map of magnetic squashing degree (Figure 4(c)), and the boundary becomes more and more distinct as the MFR expands with time. Such expansion is also reflected in the evolution of a region with strong twist number (Figure 4(d)). The rising path of the MFR deviates from the vertical toward the east (the $-x$ direction), where the magnetic pressure is weaker than to the west (the $+x$ direction).

Starting from the initial BP point, there evolves an intersection of the QSL below the MFR, forming an X shape of increasing height and size. Such a QSL intersection is a magnetic null-point configuration in the 2D plane, while in 3D it is known as an HFT, where the highest Q values are often found, making the HFT a preferential site for current accumulation and subsequent dissipation through magnetic reconnection (Titov et al. 2002). Indeed, an intense CS forms there (with $J/B > 0.2/\Delta$, where Δ is the grid size) (compare Figures 4(a) and (c)), and it also evolves into an X shape. Moreover, magnetic reconnection is triggered in the HFT (or the CS) as indicated by the plasma flows near the CS (see Figure 5(a)), which shows a typical pattern of reconnection flows in 2D, i.e., bidirectional horizontal inflows on either side of the CS and bidirectional vertical outflows away from the X point. This reconnection along with the cusp–CS–rope configuration (see the 2D field lines in Figure 5(a)) reproduces nicely the picture of the standard flare model in 2D. Interestingly, the shape of enhanced current layer and its evolution look rather similar to the AIA images of the limb X8.2 flare in the same AR (Figure 4(b)), although the simulation is not aimed at that flare. The X8.2 flare is characterized by a bright ring enclosing a relatively dark cavity of increasing size. The coronal cavity often indicates an MFR (Gibson & Fan 2006), while its outer edge is bright because heating is enhanced there by the dissipation of the strong current in the boundary layer of the rope. Below the cavity is an even brighter cusp-shaped flare loop system, the shape of which is also seen in the current distribution in the simulation.

Evolution of the magnetic twist distribution as shown in Figure 4(d) indicates that the reconnection adds magnetic twist to the MFR (Wang et al. 2017). In Figure 6, we show the time evolution of the sum of the magnetic flux content (multiplied by twist number) of the MFR with twist number above unity. A significant increase in twisted flux with time can be seen. The twist is added to the outer layer of the rope (Figure 4(d)), while the central part of the rope maintains the pre-flare twist numbers.

In 3D, the MFR's surface (or boundary) is rather complex, but an arched tube structure can be seen from the 3D QSLs (Figure 7 and the online animated version), within which the magnetic twist is distinctly stronger than that of the ambient flux (Figure 8, see also the QSL and twist distribution on the bottom surface in Figures 9(a) and (b)). With the rising of the MFR body, its conjugated legs are rooted in the far-side polarities P1/N1, while its pre-flare connections to P0 and N0 are cut by the reconnection. Consequently, the initial elongated distribution of magnetic twist along the main PIL becomes coherent in the two feet of the rope, which expand in size with time (Figure 9(b) and the online animated Figure 10). Both feet are rather irregular: while the southern one has a high-Q boundary, which is highlighted by brightening in AIA 304 Å (Figure 9(d)), the northern one is even more complex: it initially has a closed boundary but quickly splits into two fractions due to the mixed magnetic polarities there. As can be seen in the online animated Figure 10, the southern foot expands from the initial closed QSL that separates the P1–N1 flux from those of other connections. Thus the initial P1–N1 flux provides a seed for the subsequent erupting rope, and the weakly twisted seed flux remains in the rope's core, which is surrounded by highly twisted flux.

The 3D magnetic field lines of the evolving MFR are shown in Figure 12(a). The expansion of the tube-like flux rope can be visualized by the evolution of the magnetic field lines traced from the rope's high-Q boundary (Figure 12(b)). This expansion find its signatures in an EUV hot channel observed by *SDO*/AIA 94 Å from above (see Figure 12(c)). Two bright edges are observed to expand away from the main PIL (see also the the online animated Figure 13), which agrees well with the expanding surface of the simulated rope (as seen from the same view angle, Figure 12(b)). Such EUV hot channels are often deemed to be associated with erupting MFRs (Cheng et al. 2012; Zhang et al. 2012), and here it is suggested to correspond specifically to the surface or topological interface of the MFR. No writhing signature of the rope appears, as seen in both the simulation and the observation, indicating that the KI did not occur. Thus the TI is probably the driving mechanism of the eruption, at least in the early stage of this eruption.

After the onset of the eruption, the footpoint of the BPSS, which is aligned along the main PIL, starts to bifurcate (Figure 9(a) and the online animated Figure 10). The bifurcation nicely matches the two parallel flare ribbons departing the PIL (Figure 9(d) and the online animated Figure 13). This is associated with the transformation of the BPSS into the HFT, as the MFR rises and develops into a coherent structure (Figures 4 and 12). The dynamic flare

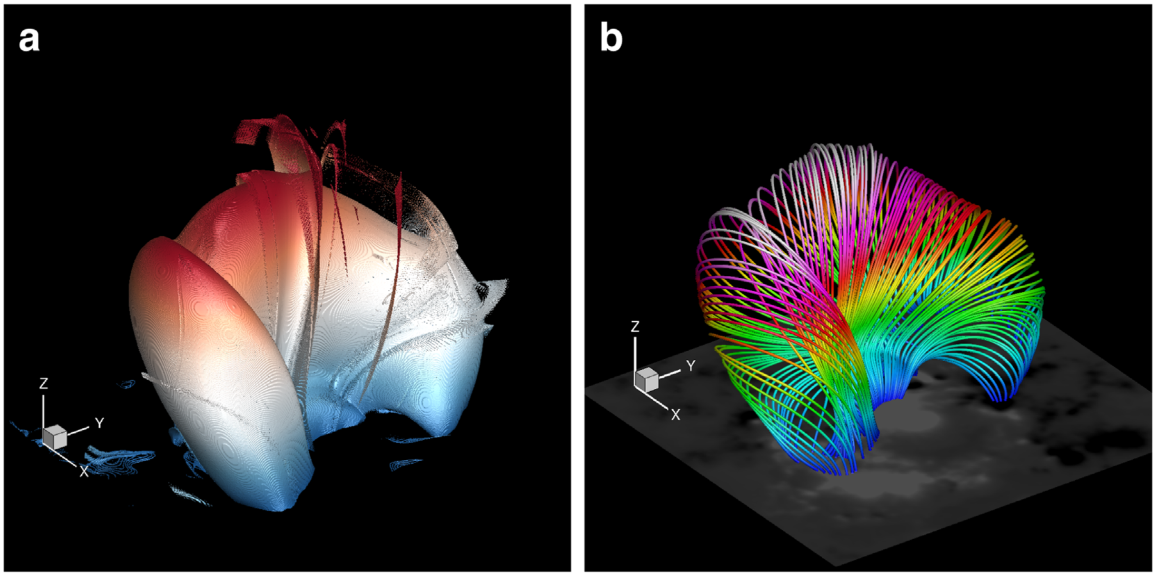

Figure 7. 3D structure of the QSLs that wrap the erupting MFR at simulation time $t = 1$. (a) The isosurface of $Q = 1000$. (b) Sampled magnetic field lines that form the QSL. The colors denote the value of height z. A animation of the rotating view of this structure is provided in online. An animation of a moving slice crossing through the MFR in the y direction is available in Figure 8.

(An animation of this figure is available.)

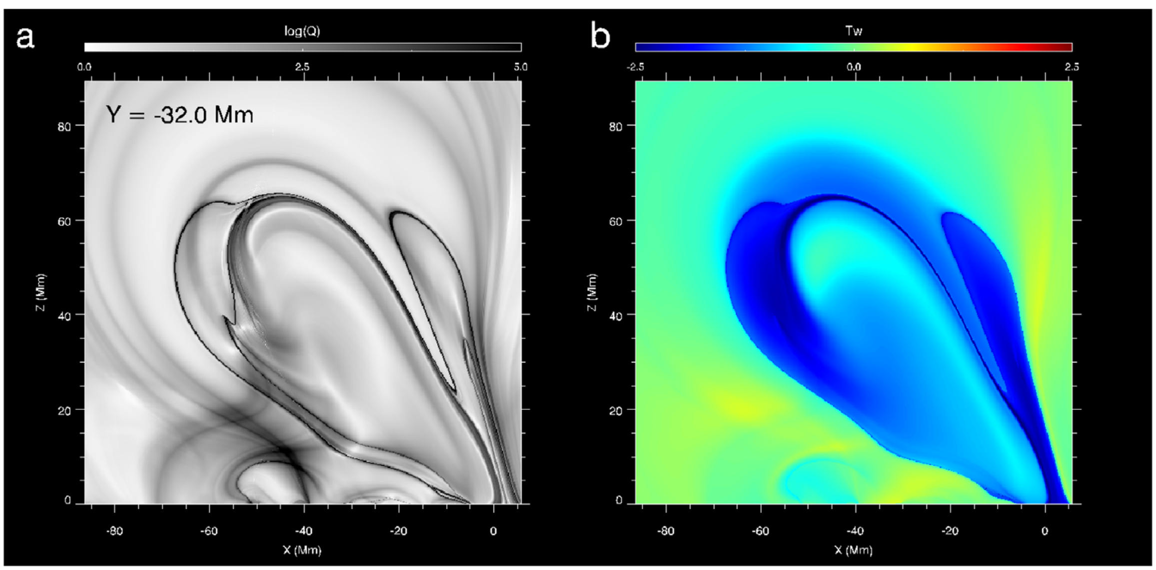

Figure 8. An animation of a moving slice crossing through the MFR in the y direction, which shows the structure of the QSL and the twist number in the MFR, is provided online. The static figure shows the structures at $Y = -32$ Mm and the full animation runs from $Y = -72$ to $+72$ Mm.

(An animation of this figure is available.)

ribbons reflect the instantaneous footpoints of magnetic field lines undergoing reconnection. These field lines form the QSL boundary of the MFR and pass through the CS (or the HFT) below the rising rope. Thus, the flare ribbons, the footpoints of field lines threading the CS, and the footpoint of the HFT are co-spatial, as demonstrated in Figure 9. The reconnection in 3D occurs in a tether-cutting-like fashion. As illustrated in Figures 5(b) and (c), the reconnecting field lines (red and green) are highly sheared and their inner footpoints below the rope (white) are close to each other, where the field directions change abruptly across the CS. The reconnection will produce a long twisted field line winding the rope and a short post-flare loop (yellow), therefore "cutting loose" the sheared field lines from their original anchors below the rope.

In Figure 14, the separation speed of the two main ribbons from the simulation is compared with that from observation: the modeled speed, 50–70 km s^{-1}, is approximately 3–5 times faster than the observed one (10–20 km s^{-1}). The reconnection rate, as measured by the ratio of inflow speed to the local Alfvén speed (i.e., the inflow Alfvén Mach number), is 0.05–0.1 in the MHD simulation, which is comparable to the values estimated from direct observational analysis of various

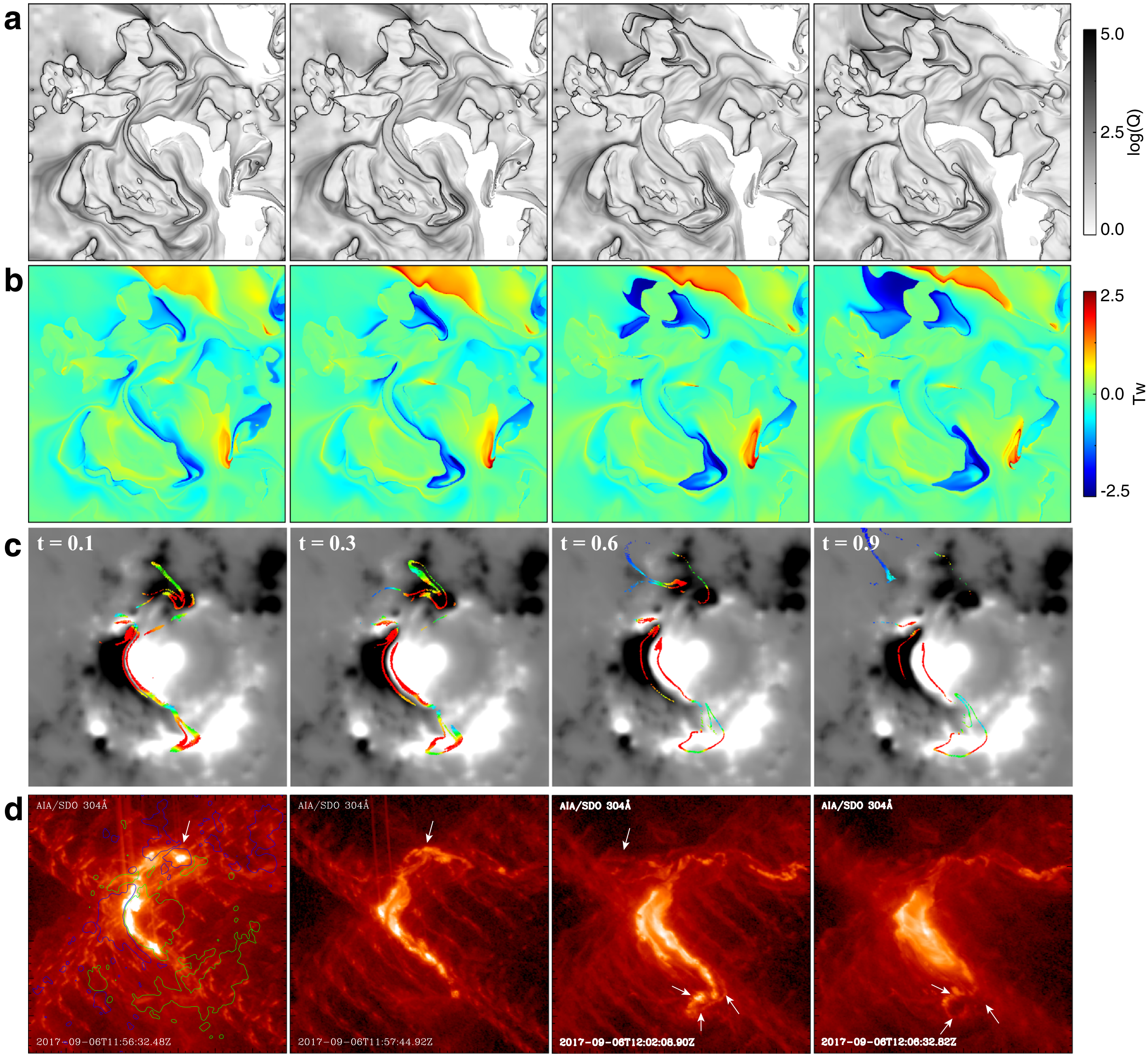

Figure 9. Structures and evolution at the bottom surface. (a) Magnetic squashing degrees. (b) Magnetic twist numbers. An animation of the temporal evolution of the magnetic squashing degree and twist number is provided in Figure 10. (c) Magnetic footpoints (colored dots) of the field lines that are traced from the CS to the bottom surface. The colors represent the strength of local magnetic field, red for strong and blue for weak. (d) *SDO*/AIA 304 Å images of the flare ribbons. The arrows denote the two weak ribbons that form in the far-side polarities P1 and N1. An animation of the evolution of the flare ribbon is provided in Figure 11. The ribbons as observed in this channel look rather diffuse, but the AIA UV channels of 1600 and 1700 Å are overexposed in this flare.

flares (Su et al. 2013; Sun et al. 2015). Thus, the real value of the reconnection rate for this X9.3 flare should be 0.01–0.03, if we divide the simulated reconnection rate by the ratio of the simulated ribbon separation speed to the observed one. It is plausible that our model produces reconnection much faster than the observed rate because the numerical resistivity is much larger than that of the real corona (see Section 2.3).

In the simulation, we can precisely calculate the reconnection flux, which is the magnetic flux swept by the main ribbons of the QSL footpoints. In Figure 15, we compare the temporal evolution of the reconnection flux with *GOES* soft X-ray flux at 1–8 Å, which can be used to represent the time profile of the flare energy release. In the simulation of one time unit $\tau = 90$ s, a total flux of 2×10^{21} Mx reconnects, and the temporal rate of the reconnection flux impulsively reaches its peak at ∼30 s, and then decreases. It can be seen that the profile of soft X-ray flux from 11:55 UT to 12:00 UT is comparable with that of the reconnection flux (compare Figures 15(b) and (d)). The ratio of the observed time (5 minutes) to our simulated one (90 s), is also consistent with the ratio of the simulated ribbon separation speed to the observed one. Furthermore, the profile of the reconnection rate looks rather similar to the time derivative of the X-ray flux (compare Figures 15(c) and (e)), despite the fact that the latter increases less rapidly than the

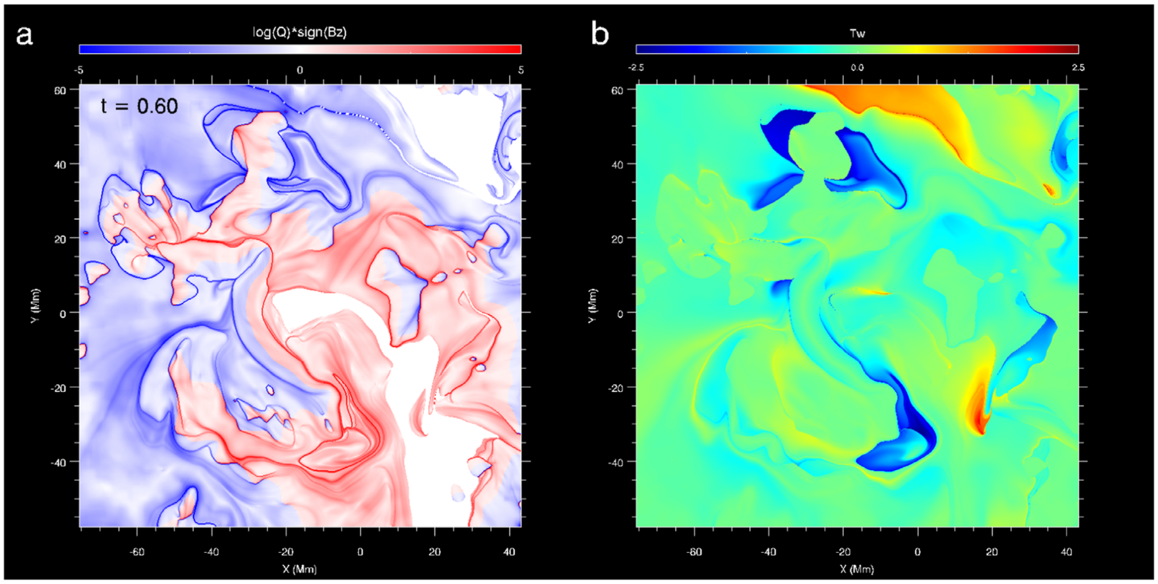

Figure 10. An animation of the temporal evolution of the magnetic squashing degree (left panel) and twist number (right panel) is provided online. The static figure shows the structures at $t = 0.6$ and the full animation runs from $t = 0$ to 1.

(An animation of this figure is available.)

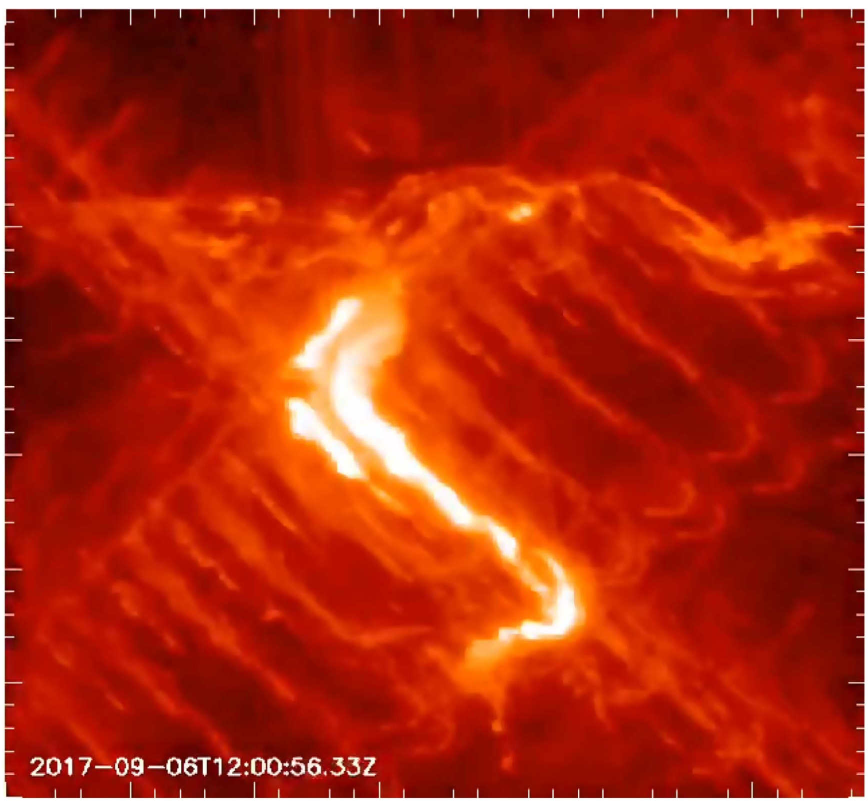

Figure 11. An animation of the *SDO*/AIA 304 Å images of the ribbon evolution is provided online. The animation runs from 11:56 to 12:15 UT on 2017 September 6.

(An animation of this figure is available.)

simulated one. This indicates that the simulation reproduced the early process of flare-energy impulsive release, except that the numerical model enhanced the reconnection rate by several times.

In addition to the double ribbons parallel to the main PIL, relatively weak ribbons extend to the two remote polarities, P1 and N1, forming a nearly closed ring at P1, similar to the observation in Wang et al. (2017), while its counterpart at N1 is

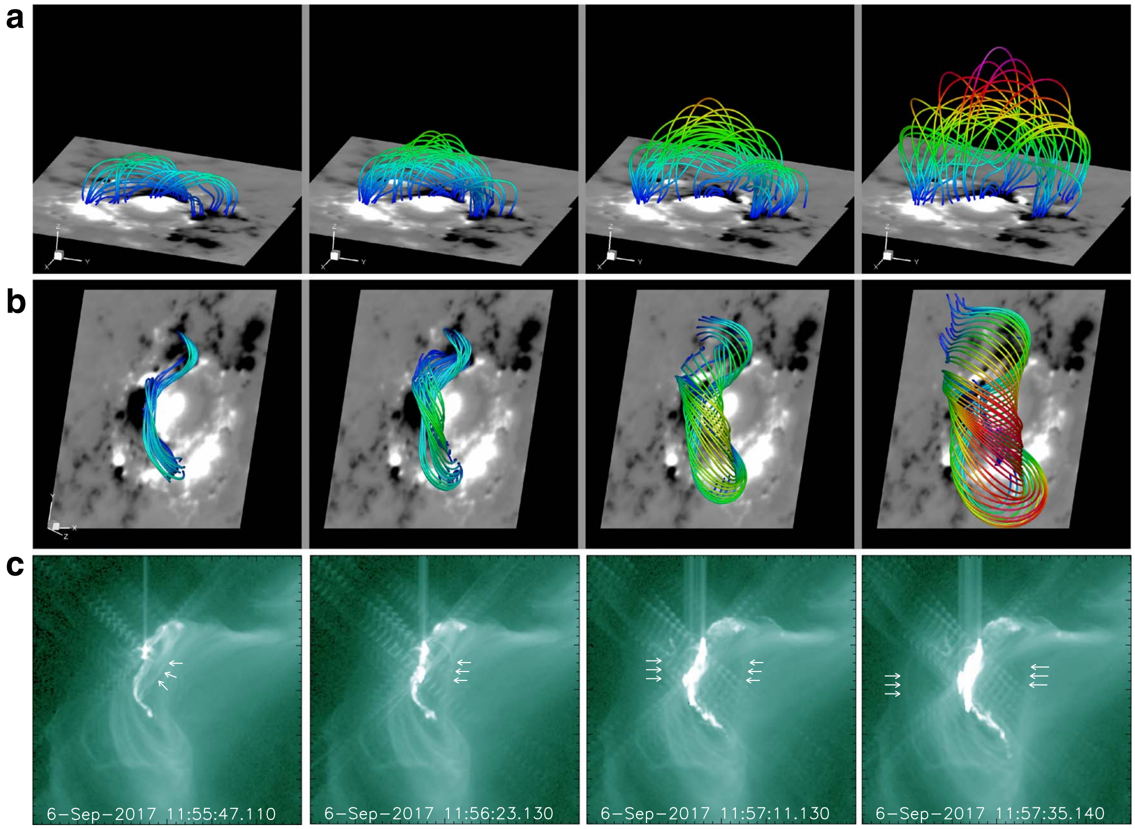

Figure 12. The eruptive structure in 3D and a comparison with *SDO*/AIA observation. (a) Side view of sampled magnetic field lines of the erupting MFR. The magnetic field lines are false-colored by the value of height z for a better visualization. The bottom surface is shown with the photospheric magnetogram. (b) Magnetic field lines that form the surface of the MFR (see the animated version of Figure 7 for a 3D rotation view of these field lines, as well as the 3D structure of the QSL). The view angle is arranged to be the same as that of the *SDO*. (c) *SDO*/AIA 94 Å observations of the eruption process. Two sets of arrows mark the two expanding edges, presumably corresponding to the expanding surface of the MFR. Such expanding features can be seen more clearly in the animated Figure 13.

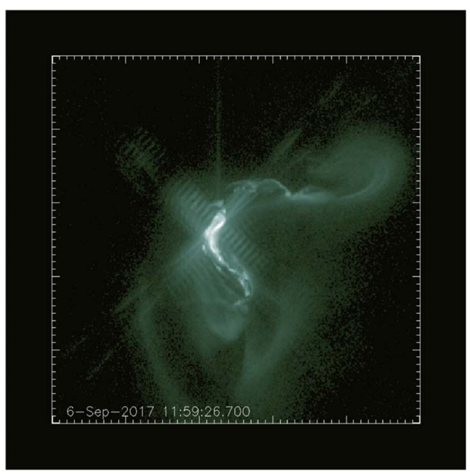

Figure 13. An animation of the *SDO*/AIA 94 Å observations of the eruption process is provided online. The animation runs from 11:50 to 12:00 UT on 2017 September 6.
(An animation of this figure is available.)

rather complex. These ribbons are produced by reconnection-released energy depositing at the far ends of the reconnecting field lines threading the CS, therefore constituting the boundary of the MFR's feet, which expands with the separation of the double ribbons (Figure 9). The expansion is attributed to reconnections at the CS, which add successive layers of twisted flux to the MFR. In observation, the feet of an erupting MFR are often indicated by a pair of transient coronal dimmings, resulting from plasma evacuation along the MFR legs into interplanetary space (Webb et al. 2000; Qiu et al. 2007). In Figure 5(d), an AIA 304 Å image taken before the eruption is subtracted from one taken after the eruption, and shows two distinct patches of coronal dimming at N1 and P1, which match the two feet of the modeled MFR.

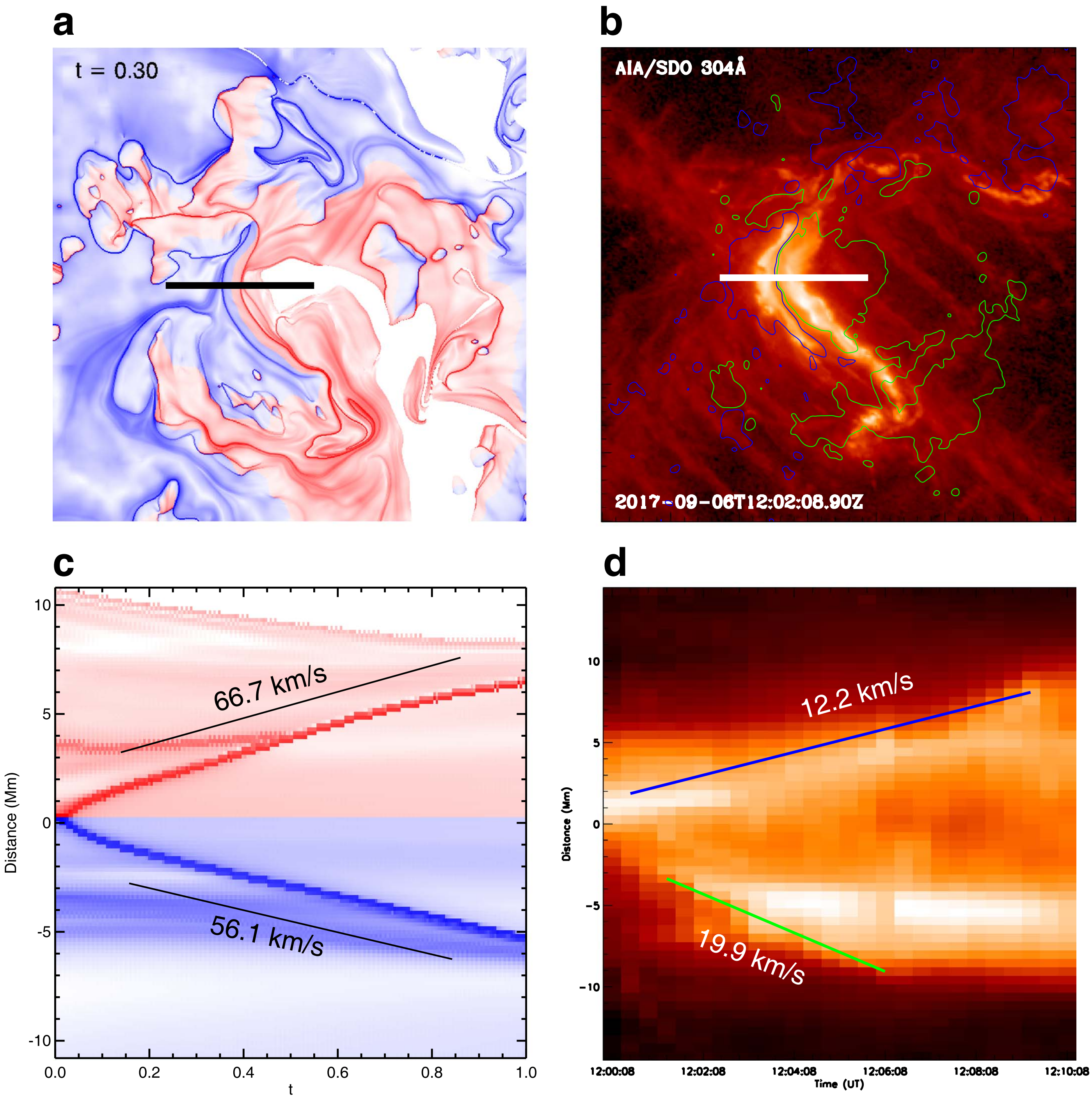

Figure 14. Comparison of flare-ribbon separation speed from MHD simulation and from observation. (a) The QSL map on the bottom at time $t = 0.3$. The black line segment denotes the location where a stacked time sequence is plotted in (c) for tracking the separation of the main QSLs that maps the reconnection footpoint. (b) *SDO*/AIA 304 Å image of the flare ribbons. In the same way, the white line segment is the location of the time stack shown in (d), which shows the separation motion of the main flare ribbons. The lines shown in (c) and (d) represent approximately the speeds of the ribbons.

4. Conclusion

In this paper, through a combination of observational data and numerical simulation, we have revealed the evolution of the topology of the magnetic configuration associated with a great eruptive flare, the largest one in solar cycle 24. Reconstruction of the coronal magnetic field immediately prior to the flare results in a complex MFR system that consists of multiple bundles of field lines with different connections and degrees of twist. Owing to a strongly distorted, quadrupolar photospheric magnetic configuration, the main body of the MFR forms a C shape, unlike the more typically observed sigmoidal one. Magnetic field lines of the MFR run horizontally over the strongly sheared PIL in the core of the AR. The bottom of the rope is attached to the photosphere, resulting in BPs along the PIL. Analysis of the decay index of the background potential field in the vicinity of the MFR shows that a major part of the MFR already enters the TI domain.

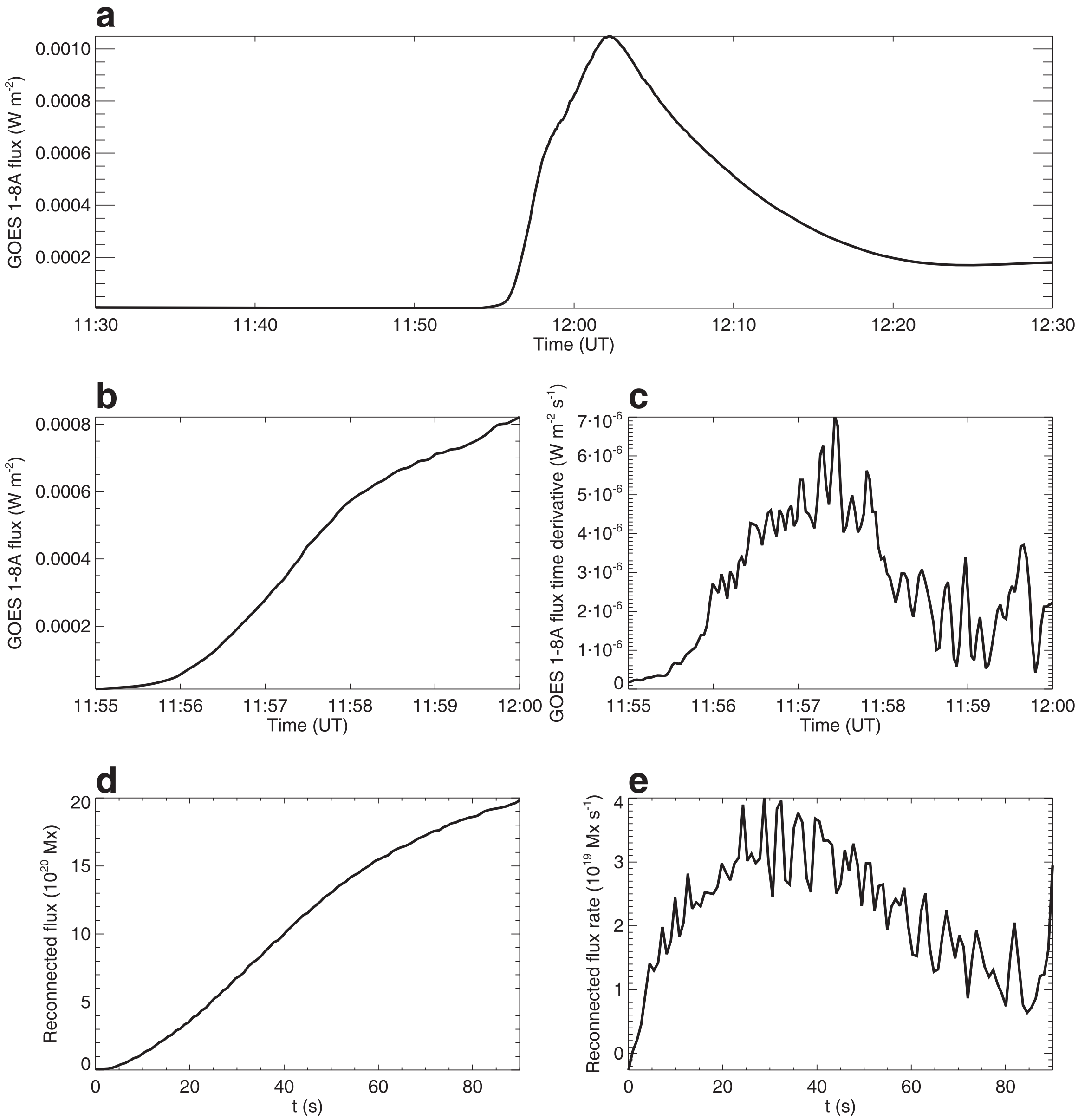

Figure 15. Reconnected flux as compared with the profile of X-ray flux. (a) The *GOES* soft X-ray flux (1–8 Å) from 11:30 to 12:30, 2017 September 6. (b) Same as (a) but for a small interval of 5 minutes starting from the beginning of the flare. (c) The time derivative of the flux shown in (b). (c) The temporal evolution of reconnected flux in the simulation. (d) Time derivative of the reconnection flux curve, i.e., reconnection flux rate.

The unstable nature of the pre-flare magnetic field results in fast expansion and rising of the MFR in the MHD simulation as initialized by the reconstruction data. In the wake of the rising MFR, an HFT comes into being from the BPs, resulting in an intersection of the QSL that warps the rope. Strong current density thus accumulates in the HFT, forming a CS, and reconnection is consequently triggered there. Magnetic twist is sequentially built up on the outer layer of the rope through reconnection of the field lines there. The modeled magnetic configuration and evolution are found to be consistent with observed EUV features of the eruption, such as the expanding hot channels that presumably result from the enhanced emission in the MFR-related QSL, the dark cavity with a bright edge that corresponds to the cross section of the rope (although imaged for another flare of the same AR), and the coronal dimming in the feet of the rope. Most importantly, by tracing the newly reconnected field lines from the CS to the bottom surface, we have reproduced the location of two main flare ribbons as well as their separation. We estimated the average reconnection rate of the flare to be 0.01–0.03 by comparing the simulated ribbon separation speed with the observed one. Furthermore, the temporal profile of the simulated reconnection flux is comparable to the observed soft X-ray flux. In addition to the main ribbons, there are relatively weak flare ribbons of closed shape extending to the two feet of the rising rope, which is successfully matched by the far-end footpoints of the newly reconnected field lines or the footpoints of the MFR-related QSL. The areas enclosed by these ribbons increase gradually as an increasing amount of flux joins the MFR through the reconnection.

The significance and also uniqueness of our simulation is that we did not use any prior assumption on the magnetic configuration of the eruptive structure. The pre-flare flux-rope complex is reconstructed directly from the vector magnetogram, and its evolution to a coherent MFR is self-consistently reproduced by the MHD model. This is distinct from many other data-constrained simulations of solar eruption, which are made based on the prior assumption of the existence of an MFR. For example, in a series of papers (Savcheva et al. 2015, 2016; Janvier et al. 2016), an MFR with its axis roughly fitting the observed filament is inserted into a potential field environment, and consequently the bottom boundary does not match the observed magnetogram. In the works of Inoue et al. (2015, 2018), an MFR is made by reconnection between sheared magnetic arcades that is reconstructed by the NLFFF model of the pre-flare corona. By including an ad hoc, current-dependent anomalous resistivity, reconnection occurs above the strongly sheared neutral line. It is unclear whether the flux rope and subsequent flare reconnection can be reproduced without the anomalous resistivity in their model. However, unlike the simulations of Savcheva et al. (2016), Inoue et al. (2018), and Török et al. (2018), which explicitly alter a stable initial field to make it unstable, here our simulation started from an already unstable field. Thus it should be noted that, because we have not investigated whether any pre-flare NLFFF configuration would be stable in our dynamic MHD model, we cannot rule out the possibility that the vector magnetograms significantly prior to (for instance, hours before) the actual flare might also produce an eruption in our model. In other words, the occurrence of an eruption in our model might not depend upon details of the input magnetogram. This issue needs to be investigated in future works for the purpose of identifying the true mechanisms that trigger eruptions.

In summary, without any prior assumption on the magnetic configuration, we reproduced the eruptive process of a great solar flare with a numerical MHD simulation based entirely on a pre-flare vector magnetogram on the photosphere. Without the simulation, it would be extremely difficult to envision the evolving magnetic topology, although the evolution is hinted at by observational features, e.g., the originally incongruous MFR growing into a coherent structure via magnetic reconnection, which is manifested in the evolving ribbon morphology that significantly deviates from two parallel or J-shaped ribbons in the standard picture. To conclude, such a realistic model and comprehensive analysis provide a sophisticated characterization of the invisible coronal magnetic field behind the eruption, which is of the utmost importance for the eventual understanding and forecasting of solar flares/CMEs.

Data from observations are courtesy of NASA *SDO*/AIA and the HMI science teams. The computational work was carried out on TianHe-1 (A) at the National Supercomputer Center in Tianjin, China. This work is supported by the National Natural Science Foundation of China (NSFC 41822404, 41731067, 41574170, 41531073), the Fundamental Research Funds for the Central Universities (grant No. HIT.BRETIV.201901), and Shenzhen Technology Project JCYJ20170307150645407. C.J. and Q.H. also acknowledge NSF grant AGS-1650854 and NASA grant 80NSSC17K0016 for partial support. R.L. acknowledges support by NSFC 41474151, 41774150, and 41761134088. P.V. acknowledges support by an INSPIRE grant of the AORC scheme under the Department of Science and Technology of India. We are very grateful to the anonymous referee for his meaningful comments and suggestions.

ORCID iDs

Chaowei Jiang https://orcid.org/0000-0002-7018-6862
Peng Zou https://orcid.org/0000-0002-8474-0553
Xueshang Feng https://orcid.org/0000-0001-8605-2159
Qiang Hu https://orcid.org/0000-0002-7570-2301
Rui Liu https://orcid.org/0000-0003-4618-4979
P. Vemareddy https://orcid.org/0000-0003-4433-8823
Aiying Duan https://orcid.org/0000-0002-1916-1053
Pingbing Zuo https://orcid.org/0000-0003-4711-0306
Yi Wang https://orcid.org/0000-0002-7094-9794

References

Amari, T., Canou, A., & Aly, J. J. 2014, Natur, 514, 465
Amari, T., Canou, A., Aly, J.-J., Delyon, F., & Alauzet, F. 2018, Natur, 554, 211
Amari, T., Luciani, J. F., Aly, J. J., Mikic, Z., & Linker, J. 2003, ApJ, 585, 1073
Aschwanden, M. J. 2004, Physics of the Solar Corona (Berlin: Springer)
Aulanier, G., Janvier, M., & Schmieder, B. 2012, A&A, 543, A110
Aulanier, G., Török, T., Démoulin, P., & DeLuca, E. E. 2010, ApJ, 708, 314
Awasthi, A. K., Liu, R., Wang, H., Wang, Y., & Shen, C. 2018, ApJ, 857, 124
Bobra, M. G., Sun, X., Hoeksema, J. T., et al. 2014, SoPh, 289, 3549
Carmichael, H. 1964, NASSP, 50, 451
Cheng, X., Zhang, J., Saar, S. H., & Ding, M. D. 2012, ApJ, 761, 62
Demoulin, P., Henoux, J. C., Priest, E. R., & Mandrini, C. H. 1996, A&A, 308, 643
DeRosa, M. L., Schrijver, C. J., Barnes, G., et al. 2009, ApJ, 696, 1780
DeRosa, M. L., Wheatland, M. S., Leka, K. D., et al. 2015, ApJ, 811, 107
Duan, A., Jiang, C., Hu, Q., et al. 2017, ApJ, 842, 119
Fan, Y., & Gibson, S. E. 2003, ApJL, 589, L105
Fan, Y., & Gibson, S. E. 2007, ApJ, 668, 1232
Gibson, S. E., & Fan, Y. 2006, JGR, 111, A12103
Hirayama, T. 1974, SoPh, 34, 323
Hood, A. W., & Priest, E. R. 1981, GApFD, 17, 297
Huang, N., Xu, Y., & Wang, H. 2018, RNAAS, 2, 7
Inoue, S. 2016, PEPS, 3, 19
Inoue, S., Hayashi, K., Magara, T., Choe, G. S., & Park, Y. D. 2014, ApJ, 788, 182
Inoue, S., Hayashi, K., Magara, T., Choe, G. S., & Park, Y. D. 2015, ApJ, 803, 73
Inoue, S., Kusano, K., Büchner, J., & Skála, J. 2018, NatCo, 9, 174
Janvier, M., Aulanier, G., Bommier, V., et al. 2014, ApJ, 788, 60
Janvier, M., Aulanier, G., & Démoulin, P. 2015, SoPh, 290, 3425
Janvier, M., Savcheva, A., Pariat, E., et al. 2016, A&A, 591, A141
Jiang, C., & Feng, X. 2013, ApJ, 769, 144
Jiang, C., & Feng, X. 2014, SoPh, 289, 63
Jiang, C., Wu, S. T., Feng, X., & Hu, Q. 2014a, ApJL, 786, L16
Jiang, C., Wu, S. T., Yurchyshyn, V. B., et al. 2016, ApJ, 828, 62
Jiang, C., Yan, X., Feng, X., et al. 2017, ApJ, 850, 8
Jiang, C. W., & Feng, X. S. 2012, ApJ, 749, 135
Jiang, C. W., Feng, X. S., Wu, S. T., & Hu, Q. 2013, ApJL, 771, L30
Jiang, C. W., Feng, X. S., Zhang, J., & Zhong, D. K. 2010, SoPh, 267, 463
Jiang, C. W., Wu, S. T., Feng, X. S., & Hu, Q. 2014b, ApJ, 780, 55
Jiang, C. W., Wu, S. T., Feng, X. S., & Hu, Q. 2016, NatCo, 7, 11522
Kliem, B., Linton, M. G., Török, T., & Karlický, M. 2010, SoPh, 266, 91
Kliem, B., Su, Y. N., van Ballegooijen, A. A., & DeLuca, E. E. 2013, ApJ, 779, 129
Kliem, B., & Török, T. 2006, PhRvL, 96, 255002
Kontogiannis, I., Georgoulis, M. K., Park, S.-H., & Guerra, J. A. 2017, SoPh, 292, 159
Kopp, R. A., & Pneuman, G. W. 1976, SoPh, 50, 85
Kusano, K., Bamba, Y., Yamamoto, T. T., et al. 2012, ApJ, 760, 31
Lei, J., Huang, F., Chen, X., et al. 2018, JGRA, 123, 3217
Li, Y., Xue, J. C., Ding, M. D., et al. 2018, ApJL, 853, L15
Linker, J. A., Mikić, Z., Lionello, R., et al. 2003, PhPl, 10, 1971
Liu, R., Kliem, B., Titov, V. S., et al. 2016, ApJ, 818, 148
Liu, Y., Sun, X., Török, T., Titov, V. S., & Leake, J. E. 2017, ApJL, 846, L6
Low, B. C., & Lou, Y. Q. 1990, ApJ, 352, 343
MacNeice, P., Antiochos, S. K., Phillips, A., et al. 2004, ApJ, 614, 1028
Mei, Z. X., Keppens, R., Roussev, I. I., & Lin, J. 2018, A&A, 609, A2
Mikic, Z., & Linker, J. A. 1994, ApJ, 430, 898
Moore, R. L., Sterling, A. C., Hudson, H. S., & Lemen, J. R. 2001, ApJ, 552, 833
Myers, C. E., Yamada, M., Ji, H., et al. 2015, Natur, 528, 526

Powell, K. G., Roe, P. L., Linde, T. J., Gombosi, T. I., & de Zeeuw, D. L. 1999, JCoPh, 154, 284
Priest, E. R., & Forbes, T. G. 2002, A&ARv, 10, 313
Qiu, J., Hu, Q., Howard, T. A., & Yurchyshyn, V. B. 2007, ApJ, 659, 758
Roussev, I. I., Forbes, T. G., Gombosi, T. I., et al. 2003, ApJL, 588, L45
Savcheva, A., Pariat, E., McKillop, S., et al. 2015, ApJ, 810, 96
Savcheva, A., Pariat, E., McKillop, S., et al. 2016, ApJ, 817, 43
Schou, J., Scherrer, P. H., Bush, R. I., et al. 2012, SoPh, 275, 229
Schrijver, C. J., DeRosa, M. L., Metcalf, T., et al. 2008, ApJ, 675, 1637
Schrijver, C. J., De Rosa, M. L., Metcalf, T. R., et al. 2006, SoPh, 235, 161
Shibata, K., & Magara, T. 2011, LRSP, 8, 6
Sturrock, P. A. 1966, Natur, 211, 695
Su, Y., Veronig, A. M., Holman, G. D., et al. 2013, NatPh, 9, 489
Sun, J. Q., Cheng, X., Ding, M. D., et al. 2015, NatCo, 6, 7598
Sun, X., Bobra, M. G., Hoeksema, J. T., et al. 2015, ApJL, 804, L28
Sun, X., Hoeksema, J. T., Liu, Y., et al. 2012, ApJ, 748, 77
Sun, X., & Norton, A. A. 2017, RNAAS, 1, 24
Titov, V. S., & Démoulin, P. 1999, A&A, 351, 707
Titov, V. S., Hornig, G., & Démoulin, P. 2002, JGRA, 107, 1164
Titov, V. S., Priest, E. R., & Demoulin, P. 1993, A&A, 276, 564
Török, T., Downs, C., Linker, J. A., et al. 2018, ApJ, 856, 75
Török, T., & Kliem, B. 2005, ApJL, 630, L97
Török, T., Kliem, B., & Titov, V. S. 2004, A&A, 413, L27
Török, T., Leake, J. E., Titov, V. S., et al. 2014, ApJL, 782, L10
Török, T., Temmer, M., Valori, G., et al. 2013, SoPh, 286, 453
van Ballegooijen, A. A. 2004, ApJ, 612, 519
van Ballegooijen, A. A., Deluca, E. E., Squires, K., & Mackay, D. H. 2007, JASTP, 69, 24
Vemareddy, P. 2017, ApJ, 851, 3
Wang, H., Yurchyshyn, V., Liu, C., et al. 2018, RNAAS, 2, 8
Wang, W., Liu, R., Wang, Y., et al. 2017, NatCo, 8, 1330
Warren, H. P., Brooks, D. H., Ugarte-Urra, I., et al. 2018, ApJ, 854, 122
Webb, D. F., Lepping, R. P., Burlaga, L. F., et al. 2000, JGR, 105, 27251
Wiegelmann, T., & Neukirch, T. 2006, A&A, 457, 1053
Wyper, P. F., Antiochos, S. K., & DeVore, C. R. 2017, Natur, 544, 452
Yan, X. L., Wang, J. C., Pan, G. M., et al. 2018, ApJ, 856, 79
Yang, S., Zhang, J., Zhu, X., & Song, Q. 2017, ApJL, 849, L21
Zhang, J., Cheng, X., & Ding, M.-D. 2012, NatCo, 3, 747